Growth model for ramified electrochemical deposition in the presence of diffusion, migration, and electroconvection

Guillermo Marshall
Consejo Nacional de Investigaciones Cientificas, Comision Nacional de Energia Atomica and Universidad de Buenos Aires, 1429 Buenos Aires, Argentina

Pablo Mocskos
Universidad de Buenos Aires, 1429 Buenos Aires, Argentina

(Received 11 December 1995; revised manuscript received 9 April 1996)

A growth pattern formation model for the macroscopic description of ramified electrochemical deposition is presented. The model describes the diffusive, migration and electroconvective motion of ions and its deposition in thin cells through the evolutionary two-dimensional Nernst-Planck equations for cation and anion concentration, the Poisson equation for the electric field, the Navier-Stokes equations for the laminar fluid flow and a dielectric breakdown model scheme for the random deposition of ions. A new set of dimensionless numbers governing the model regimes is introduced. We present numerical results showing that, for a given set of dimensionless numbers, the electroconvective forces produce vortex-tip interaction yielding a basic growth pattern formation mechanism, i.e., tip splitting and fanning. This mechanism gives a reasonable picture of reality. [S1063-651X(96)01610-8]

PACS number(s): 68.70.+w, 82.45.+z, 47.65.+a, 02.70.Bf

I. INTRODUCTION

Growth pattern formation, that is, the unstable growth of interfaces, is a common phenomenon in a wide range of problems from physics to biology. It produces complex geometries of fractal or dendritic character and chaotic patterns [1–5] and has been extensively studied in the context of far from equilibrium phenomena.

An example is electrochemical deposition (ECD) of ramified metallic clusters in thin cells. The quasi-two-dimensional electrolytic cell consists of two glass plates sandwiching two parallel electrodes and an electrolyte. A voltage difference or a current applied between electrodes produces a ramified deposit. The main variables controlling the experiment are solution concentration, voltage difference, and cell thickness. Literature shows that when these are varied growth patterns ranging from fractal to dense-branched aggregates can be obtained. The morphology variation has not yet been fully understood.

While the general equations governing ECD with fixed electrodes (describing the interaction of fields due to salt ions concentration gradients, migration, and electroconvection) have been analyzed and simulated since long ago [6], the study and simulation of ECD with moving electrodes started in the 1980s, greatly stimulated by the development of fractal geometry. Pioneering work at that time gave rise to one field models, the so called Laplacian growth models, such as the diffusion-limited aggregation [7] and the dielectric breakdown [8] models (DBM). Subsequent extensions of the diffusion-limited aggregation model [9–14] aimed at the inclusion, in the one field model, of migration or electroconvection field effects. A one field model, however, cannot describe the cooperative effects of the various nonlinear fields involved and is therefore severely limited.

In recent years, considerable advance was achieved in the understanding of ECD as a function of the control parameters through theoretical analysis and physical and numerical experiments [15–31]. In particular, the study of ECD with a one-dimensional (1D) model of the set of electrohydrodynamic equations describing the coupling of migration, diffusion, and electroconvection fields revealed the existence of a very thin boundary layer around the growing electrodeposits where electroneutrality is violated [15]. This layer, that produces a convective motion on the fluid, is modeled as a charge concentrated at the tips of the growing deposit [19]. Experimental results and an analysis of ECD with dense-branched morphology were presented in [20], [22], and a mechanism for morphology variations stressing the importance of electroconvection effects was proposed. Very recently the role of convection arising from concentration gradients in ECD growth was clearly established [31].

The first attempt towards a global macroscopic description of ECD taking into account the main transport mechanisms [32] consists in a 2D model for cation concentration with a stochastic rule for the random deposition of cations. The electroconvective forces were modeled as an array of Dirac-δ forces distributed over the tips of the growing aggregate, and electroneutrality assumed valid in the remaining region. This model gave reasonable qualitative results but it was limited because of the artificial coupling between electroconvective forces and local charges near the growing tips.

Here, extending the results of [32], we construct a more realistic transport model, consisting in the Nernst-Planck equations for the concentration of cations and anions coupled to an equation for the electric potential and the Navier-Stokes equations for the solvent, and a discretized version of that model in the context of a DBM scheme. We also perform a dimensional analysis that notably simplifies the otherwise large number of parameters.

The plan of the paper is the following. In Sec. II we examine the physics of ECD and the growth model describing it. The third section deals with the dimensional analysis.

The fourth presents a 1D approximation of the previous system, the fifth a 2D approximation with fixed electrodes, and the sixth the inclusion of the aggregation process. The last section draws some general conclusions.

II. THE PHYSICS AND MATHEMATICS OF THE GROWTH MODEL

The physical scenario envisaged is ECD of ramified copper clusters in a thin cell, with an unsupported binary electrolyte and with constant voltage applied between electrodes [30]. The main transport mechanisms are diffusion, migration, and electroconvective motion of the ions in a space-time dependent incompressible viscous fluid. Secondary chemical reactions, density gradients, or heat transfer are not considered here. Initially the electrolyte is electrically neutral everywhere, with uniform concentration of cations and anions in space. Applying a voltage difference between electrodes, cations move toward the cathode where they are discharged and aggregate. Anions move toward the anode where they pile up since they cannot exit the solution. Near the cathode, a positive charge is generated as a result of cation and anion movements and the fact that anions are not replaced. Experiments show that the front of the deposit advances at the same rate as anions migrate towards the anode. Near the anode, electroneutrality is maintained by cations entering the solution from the dissolving anode.

Experimental measurements and theory show that the electrolyte near the tips of the aggregation is subject to a very large local electric field, of the order of $E_0 = 1\text{V}/10\ \mu\text{m} = 10^3$ V/cm [19], which produces the movement of the fluid due to the electroconvection effect (Coulomb forces). The motion consists in two contrarotative vortices attached to the tip and moving solidarily with it. The electrolyte is neutral everywhere except at the tip, hence the Coulomb forces only act when the liquid reaches the tip. In summary, the Coulomb forces have a compact support. This is in contrast with the Rayleigh-Benard thermal convection problem in which the gravitational force acts uniformly over the fluid.

The physical model is described by the Nernst-Planck equations for the concentration of the copper ions subject to diffusion, electroconvection, and migration fields, the equation for electrostatic potential and the Navier-Stokes equations for the solvent. These equations are [6]

$$\frac{\partial C_i}{\partial t} = -\boldsymbol{\nabla}\cdot\mathbf{j}_i \quad i=1,2, \tag{1}$$

$$\mathbf{j}_i = -\mu_i C_i \boldsymbol{\nabla}\phi - D_i \boldsymbol{\nabla} C_i + C_i \mathbf{v}, \tag{2}$$

$$\nabla^2\phi = \frac{F}{\epsilon}\sum_i z_i C_i, \tag{3}$$

$$\frac{\partial \mathbf{v}}{\partial t} + \mathbf{v}\cdot\boldsymbol{\nabla}\mathbf{v} = -\frac{1}{\rho}\boldsymbol{\nabla}P + \nu\nabla^2\mathbf{v} + \frac{\mathbf{f}}{\rho}, \tag{4}$$

$$\boldsymbol{\nabla}\cdot\mathbf{v} = 0. \tag{5}$$

Here, C_i, $\mathbf{j}_i$, z_i, μ_i, and D_i are the concentration, flux, charge, mobility, and diffusion constants of an ionic species i, respectively; ϕ is the electrostatic potential, F is the Faraday constant, ϵ is the permitivity of the medium, $\mathbf{v}$ is the fluid velocity, P is the pressure, ν the kinematic viscosity, and t is the time coordinate. $\mathbf{f}$ is an external force acting over the fluid and dependent of the local charge: $\mathbf{f} = e\mathbf{E}\Sigma_i z_i C_i$, where $\mathbf{E}$ is the electric field.

System (1)-(5), with appropriate initial and boundary conditions, is valid in a space-time domain defined by $\mathbf{G=[\Omega(t)x(0,t)]}$, where Ω is a **3D** region with boundary $\Gamma(t)$; this boundary moves with speed proportional to the norm of the flux $\mathbf{j}_i$.

Next we assume that the ECD is a quasi-two-dimensional process. This is a gross approximation of reality, only justified on the grounds of rendering system (1)–(5) more tractable. Furthermore, for convenience, system (1)–(5) is written in transport-vorticity form by taking the curl of the Navier-Stokes equations (4) and introducing the vorticity ω and stream function ψ, thus eliminating the pressure. The x-y coordinate in the horizontal plane assumes the positive x axis in the west-east direction, and the positive y axis in the south-north direction (the positive z axis, normal to the x-y plane, points to the reader; hence, gravity points in the negative z direction). The cathode and anode lie, in the x-y plane, at $y=0$ and $y=d$, respectively; thus the electrical field $\mathbf{E}$ is parallel to the y direction and negative. The system now becomes

$$\frac{\partial C}{\partial t} + u_C^*\frac{\partial C}{\partial x} + v_C^*\frac{\partial C}{\partial y} = D_C\nabla^2 C + \mu_C C\nabla^2\phi, \tag{6}$$

$$\frac{\partial A}{\partial t} + u_A^*\frac{\partial A}{\partial x} + v_A^*\frac{\partial A}{\partial y} = D_A\nabla^2 A - \mu_A A\nabla^2\phi, \tag{7}$$

$$\nabla^2\phi = -\frac{Fe}{\epsilon}f, \tag{8}$$

$$\frac{\partial \omega}{\partial t} + u\frac{\partial \omega}{\partial x} + v\frac{\partial \omega}{\partial y} = \nu\nabla^2\omega - \frac{e}{\rho}\left(\frac{\partial f}{\partial x}\frac{\partial \phi}{\partial y} - \frac{\partial f}{\partial y}\frac{\partial \phi}{\partial x}\right), \tag{9}$$

$$\nabla^2\psi = -\omega. \tag{10}$$

In (6)–(10) C and A are cation and anion concentrations, ω and ψ are the vorticity and stream functions, u and v are fluid velocities, $u_C^* = u - \mu_C(\partial\phi/\partial x)$, $u_A^* = u + \mu_A(\partial\phi/\partial x)$, $v_C^* = v - \mu_C(\partial\phi/\partial y)$ and $v_A^* = u + \mu_A(\partial\phi/\partial y)$ are compound velocities due to migration and electroconvection, and $f = z_C C - z_A A$ is a scalar forcing function. Written in this form it is clear the role played by migration and electroconvection in the advection of the fluid.

III. A DIMENSIONAL ANALYSIS

With the aim of reducing the complexity of the problem described by system (6)–(10), as is common in the related literature ([33–35]), we perform a dimensional analysis, introducing the following new variables :

$$x' = x/x_0; \quad y' = y/x_0; \quad u' = u/u_0; \quad v' = v/u_0;$$

$$C' = C/C_0; \quad A' = A/C_0; \quad \phi' = \phi/\phi_0;$$

where the variables with subindex are reference values later defined. System (6)–(10) becomes

$$\frac{\partial C'}{\partial t'}+u_C'^*\frac{\partial C'}{\partial x'}+v_C'^*\frac{\partial C'}{\partial y'}=\frac{1}{\mathrm{Re}\,\mathrm{Sc}_C}\nabla^2 C'+\frac{1}{\mathrm{Re}\,M_C}C'\nabla^2\phi', \tag{11}$$

$$\frac{\partial A'}{\partial t'}+u_A'^*\frac{\partial A'}{\partial x'}+v_A'^*\frac{\partial A'}{\partial y'}=\frac{1}{\mathrm{Re}\,\mathrm{Sc}_A}\nabla^2 A'-\frac{1}{\mathrm{Re}\,M_A}A'\nabla^2\phi', \tag{12}$$

$$\nabla^2\phi'=-\frac{1}{\mathrm{Po}_C}C'+\frac{1}{\mathrm{Po}_A}A', \tag{13}$$

$$\frac{\partial\omega'}{\partial t'}+u'\frac{\partial\omega'}{\partial x'}+v'\frac{\partial\omega'}{\partial y'}=\frac{1}{\mathrm{Re}}\nabla^2\omega'+\frac{1}{\mathrm{Fr}_C}\left(\frac{\partial C'}{\partial y'}\frac{\partial\phi'}{\partial x'}-\frac{\partial C'}{\partial x'}\frac{\partial\phi'}{\partial y'}\right)+\frac{1}{\mathrm{Fr}_A}\left(\frac{\partial A'}{\partial x'}\frac{\partial\phi'}{\partial y}-\frac{\partial A'}{\partial y'}\frac{\partial\phi'}{\partial x'}\right), \tag{14}$$

$$\nabla^2\psi'=-\omega', \tag{15}$$

where $\mathrm{Sc}_C=\nu/D_C$ and $\mathrm{Sc}_A=\nu/D_A$ are the Schmidt numbers; $\mathrm{Re}=u_0x_0/\nu$ is the Reynolds number, $M_C=\nu/\mu_C\phi_0$ and $M_A=\nu/\mu_A\phi_0$ are a new set of dimensionless numbers relating viscous forces to electrostatic potential and migration forces; $u_C'^*=u-(1/\mathrm{Re}\,M_C)(\partial\phi'/\partial x')$, $v_C'^*=v-(1/\mathrm{Re}\,M_C)(\partial\phi'/\partial y')$, $u_A'^*=u+(1/\mathrm{Re}\,M_A)(\partial\phi'/\partial x')$ and $v_A'^*=v+(1/\mathrm{Re}\,M_A)(\partial\phi'/\partial y')$ are compound velocities due to electroconvection and migration; $\mathrm{Po}_C=(\epsilon\phi_0/x_0^2Fz_CC_0)$ and $\mathrm{Po}_A=(\epsilon\phi_0/x_0^2Fz_AC_0)$ are new dimensionless numbers relating electrostatic potential to solute concentration and $\mathrm{Fr}_C=(\rho u_0^2/ez_CC_0\phi_0)$ and $\mathrm{Fr}_A=(\rho u_0^2/ez_AC_0\phi_0)$ are the Froude numbers relating viscosity to electrostatic potential and concentration. The variable x_0 is a reference length scale to be chosen. According to the scale of the process analyzed, it may be the distance between electrodes, the separation between branches of a growing deposit, or the length of the boundary layer. The variable u_0 is a reference velocity scale that can be defined in terms of (a) $u_0=\nu/x_0$, or (b) $u_0=D/x_0$, where D is either D_A or D_C, or (c) $u_0=\mu E_0$, where μ is either μ_A or μ_C. Following case (c), assuming μ and E_0 are in the order of 10^{-4} and 10^3, respectively, an estimate of u_0 is 0.1 cm/sec, in agreement with typical experimental values.

In real experiments the following physical parameters corresponding to a solution of copper sulphate in distilled water $(0.01M)$ are used: $\mu_C=5.37\times10^{-4}$ cm^2/Vs, $\mu_A=8.29\times10^{-4}$ cm^2/Vs, $D_A=D_C=10^{-5}$ cm^2/s, $\nu=1\times10^{-2}$ cm^2/s, $z_C=z_A=2$, $T=293$ K, and $C_0=1\times10^{18}$ $1/\mathrm{cm}^3$. Choosing as reference values for $x_0=1$cm, for $u_0=0.1$cm/s and for $\phi_0=1V$, the dimensionless numbers become: $\mathrm{Re}=10$, $\mathrm{Sc}_C=\mathrm{Sc}_A=10^3$, $M_A=12.06$, $M_C=18.06$, $\mathrm{Po}_A=\mathrm{Po}_C=9.04\times10^{-11}$, and $\mathrm{Fr}_C=\mathrm{Fr}_A=1.2\times10^{-3}$. An increase in the Re number leaving all other numbers constant increases fluid convection, thus electroconvection in Eq. (14). It also increases migration (convective motion due to the electric field) in Eqs. (11) and (12). A similar effect is produced increasing the $\mathrm{Sc}_C(\mathrm{Sc}_A)$ numbers. An increase in the $\mathrm{Fr}_C(\mathrm{Fr}_A)$ numbers decreases electroconvection (fluid density and dynamic viscosity increase). An increase of the $M_A(M_C)$ numbers increases migration. A decrease in the Po_C (Po_A) number increases the source term in the Poisson equation (15) and therefore the curvature of the electric potential; this reduces the width of the boundary layer. Therefore, this number, which is orders of magnitude higher than the rest of the dimensionless numbers, is extremely important since it governs the singular perturbation nature of the whole system and, in particular, the source term in the electrostatic Poisson equation. It also plays a major role in the computational aspect of the problem.

IV. A ONE-DIMENSIONAL APPROXIMATION WITH FIXED ELECTRODES

Before embarking in the solution of the fully 2D problem we analyze a simplified 1D problem, following [15]. We consider a thin rectangular cell with a binary electrolyte, a constant potential difference applied between electrodes, and no fluid flow $(\mathbf{v}=0)$. To comply with the notation in [15], in our 1D approximation the cathode and anode are located at $x=0$ and $x=x_0$, respectively. The resulting equations, consistent with system (11) and (13) are

$$\frac{\partial C'}{\partial t'}=\frac{1}{\mathrm{Re}\,\mathrm{Sc}_C}\frac{\partial^2 C'}{\partial x'^2}+\frac{1}{\mathrm{Re}\,M_C}\frac{\partial}{\partial x'}\left(C\frac{\partial\phi'}{\partial x'}\right), \tag{16}$$

$$\frac{\partial A'}{\partial t'}=\frac{1}{\mathrm{Re}\,\mathrm{Sc}_A}\frac{\partial^2 A'}{\partial x'^2}-\frac{1}{\mathrm{Re}\,M_A}\frac{\partial}{\partial x'}\left(A\frac{\partial\phi'}{\partial x'}\right), \tag{17}$$

$$\frac{\partial^2\phi'}{\partial x'^2}=-\frac{1}{\mathrm{Po}_C}C'+\frac{1}{\mathrm{Po}_A}A'. \tag{18}$$

System (16) and (17) is written in conservation form as opposed to system (6) and (7) written in divergence form. Both are equivalent for smooth flows; however, in the presence of strong gradients the conservation form is preferred. Here, since there is no fluid flow, the reference velocity in the Reynolds number is implicitly defined in terms of the length and time reference scales. The initial conditions for $t=0$ are a linear function for the electric potential between $x=0$ and $x=x_0$, and a constant state equal to C_0 for cation and anion concentrations. The boundary conditions chosen are

$$\phi'(0)=-\frac{kT}{z_Ce\phi_0}\ln[z_CC'(0)], \tag{19}$$

$$\phi'(1)=\phi_0-\frac{kT}{z_Ce\phi_0}\ln[z_CC'(1)], \tag{20}$$

$$j_A'(0)=-\frac{1}{\mathrm{Re}\,\mathrm{Sc}_A}\frac{\partial A'(0)}{\partial x'}+\frac{1}{\mathrm{Re}\,M_A}A'(0)\frac{\partial\phi'(0)}{\partial x'}=0, \tag{21}$$

$$j_A'(1)=-\frac{1}{\mathrm{Re}\,\mathrm{Sc}_A}\frac{\partial A'(1)}{\partial x'}+\frac{1}{\mathrm{Re}\,M_A}A'(1)\frac{\partial\phi'(1)}{\partial x'}=0, \tag{22}$$

$$C'(x_0)=A'(x_0), \tag{23}$$

$$\frac{\partial C'}{\partial x'}(0)=0. \tag{24}$$

Equations (19) and (20) describe the boundary conditions for the electrostatic potential where it is assumed electrochemical equilibrium at the interface [15] (k is the Boltzmann constant and T is the temperature). Equations (21) and (22) describe the boundary conditions for anion concentration. They do not participate in the reaction; they are conserved in the cell and their flux is null. Equations (23) and (24) describe the boundary conditions for cation concentration. Here it is assumed that at $x=x_0$ the solution is electroneutral, thus cation equal anion concentration. At $x=0$, following [15], diffusion is assumed negligible. In summary, system (16)–(24) consists in a pair of parabolic equations for cation and anion concentrations and an elliptic equation for the electrostatic potential, subject to Dirichlet, Neumann, and Fourier boundary conditions.

System (16)–(18) is solved, for each time step, in a uniform rectangular lattice of size h (space step) and k (time step), using finite differences and deterministic relaxation techniques. An implicit conservative scheme of the preceeding system, in the usual notation and dropping the primes, reads

$$\frac{C_i^{n+1}-C_i^n}{k}=\frac{1}{\mathrm{Re\,Sc}_C}\left(\frac{C_{i+1}^{n+1}+C_{i-1}^{n+1}-2C_i^{n+1}}{h^2}\right)+\frac{1}{\mathrm{Re}\,M_C}\left(\frac{C_{i+1/2}^{n+1}(\phi_{i+1}^{n+1}-\phi_i^{n+1})-C_{i-1/2}^{n+1}(\phi_i^{n+1}-\phi_{i-1}^{n+1})}{h^2}\right), \tag{25}$$

$$\frac{A_i^{n+1}-A_i^n}{k}=\frac{1}{\mathrm{Re\,Sc}_A}\left(\frac{A_{i+1}^{n+1}+A_{i-1}^{n+1}-2A_i^{n+1}}{h^2}\right)-\frac{1}{\mathrm{Re}\,M_A}\left(\frac{A_{i+1/2}^{n+1}(\phi_{i+1}^{n+1}-\phi_i^{n+1})-A_{i-1/2}^{n+1}(\phi_i^{n+1}-\phi_{i-1}^{n+1})}{h^2}\right), \tag{26}$$

$$\phi_i^{n+1}=\frac{\phi_{i+1}^{n+1}+\phi_{i-1}^{n+1}-h^2 f^*}{2}, \tag{27}$$

where

$$f^*=-\frac{1}{\mathrm{Po}_C}C_i^{n+1}+\frac{1}{\mathrm{Po}_A}A_i^{n+1},$$

n is the time level. The concentration values with fractional subindex nodes are computed as the average of concentrations at neighboring integer nodes. The boundary conditions are approximated in a similar way. The finite difference scheme leads to a system of algebraic equations for each time step. This system is solved via a successive over relaxation iterative method and convergence for every time step is achieved whenever the following condition on the residual is satisfied:

$$\mathcal{R}=\max_i[w_i^{n+1,l+1}-w_i^{n+1,l}]<10^{-5};\quad w=A,C,\phi, \tag{28}$$

where l is the iteration level. Convergence of the evolutionary process towards the stationary state is achieved if

$$\mathcal{R}^*=\max_i[w_i^{n+1,l}-w_i^{n,l}]<10^{-7};\quad w=A,C,\phi. \tag{29}$$

The numerical method should be conservative, that is, it should conserve the following quantity:

$$\int_0^{x_0}A(x)dx=C_0x_0. \tag{30}$$

This is satisfied by the difference scheme utilized.

In the numerical simulations shown next we use the same physical constants as those introduced in Sec. III, except for C_0 that is set equal to $10^{10}(1/\mathrm{cm}^3)$ and $z_A(z_C)=1$ in order to compare our results with those in [15]. The resulting dimensionless numbers are $\mathrm{Re}\times\mathrm{Sc_C}=1\times10^5$, $\mathrm{Re}\times\mathrm{Sc_A}=1\times10^5$, $\mathrm{Re}\times M_C=1.8622\times10^3$, $\mathrm{Re}\times M_A=1.2063\times10^3$, $\mathrm{Po}_A=\mathrm{Po}_C=4.42\times10^{-3}$. The $\mathrm{Po}_A(\mathrm{Po}_C)$ value chosen is much higher than the real one. The use of a lower $\mathrm{Po}_A(\mathrm{Po}_C)$ value is limited by numerical stability requirements. The space and time steps are equal to 0.01 cm and 0.01 sec, respectively. The computer code was written in the C language and executed in a PC486. The initial conditions for cation and anion concentrations are uniform distributions equal to 1, and

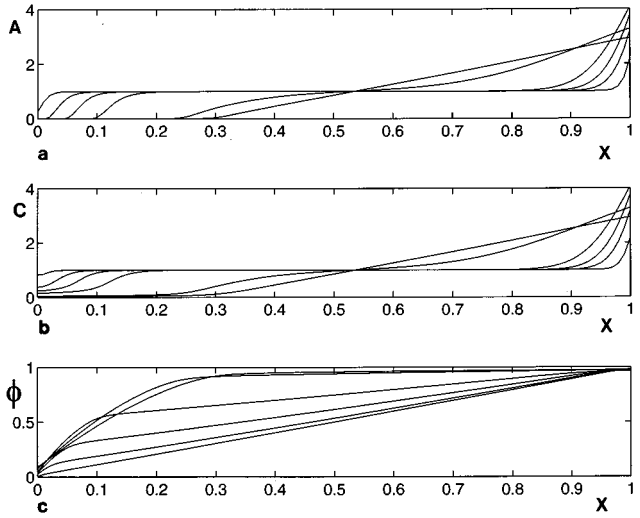

FIG. 1. Space-time evolution of the 1D approximation for (a) cation concentration, (b) anion concentration, and (c) electrostatic potential. Snapshots taken at $t=10s$, $t=50s$, $t=100s$, $t=200s$, $t=1500s$, $t=5000s$.

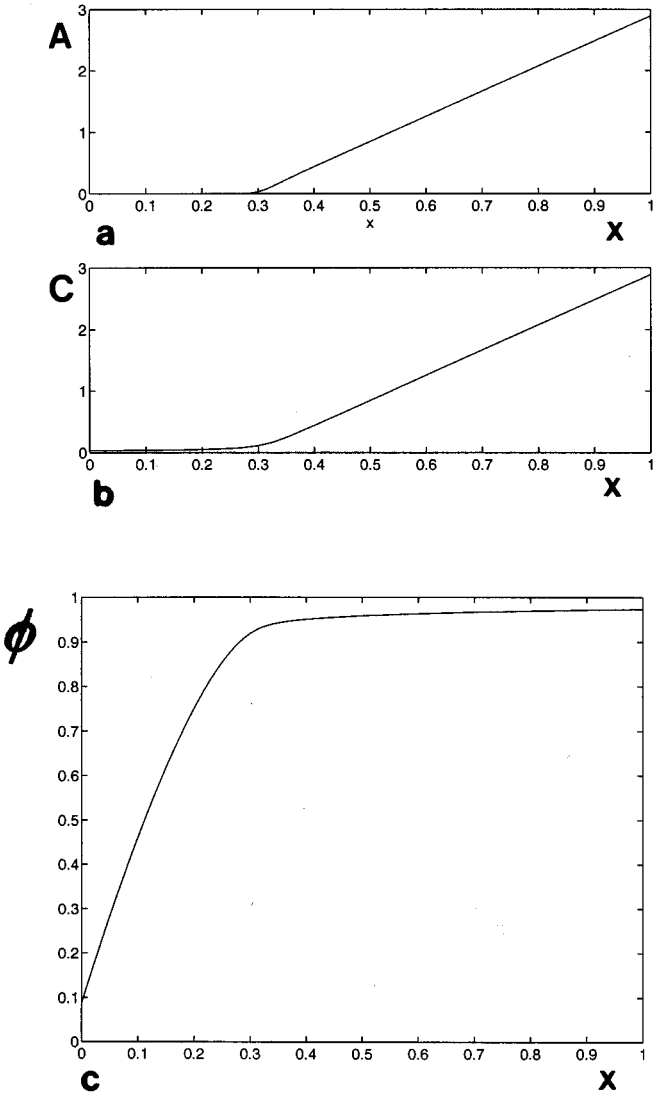

FIG. 2. Steady state solution of the 1D approximation for (a) cation concentration, (b) anion concentration, and (c) electrostatic potential ($\mathrm{Po}_A=\mathrm{Po}_C=4.42\times10^{-3}$).

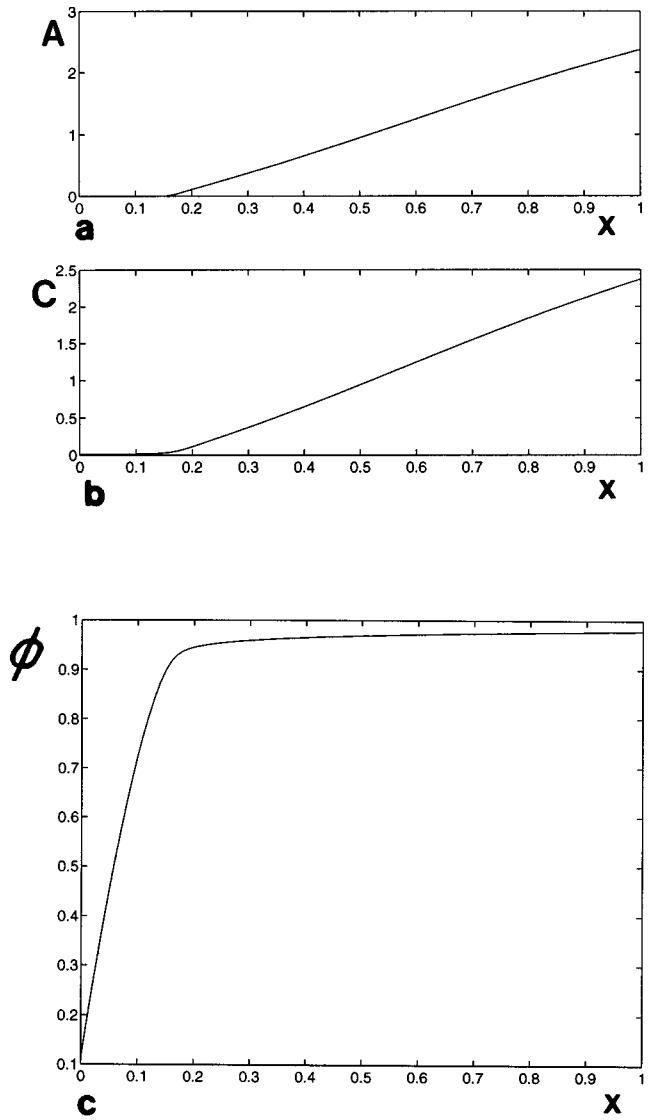

FIG. 3. 1D steady state solutions for (a) cation concentration, (b) anion concentration, and (c) electrostatic potential ($\mathrm{Po}_A=\mathrm{Po}_C=4.42\times10^{-4}$).

for the electrostatic potential a linear function between 0 and 1. Apparently, with these initial conditions the system cannot evolve. However, the ''one-dimensional electrochemical process'' is triggered at the first time step when the system automatically adjusts the conservation of anions at the cathode.

Figures 1(a), 1(b), and 1(c) shows the space-time variation of cation and anion concentrations and electrostatic potential, respectively. At the stationary state, the depletion of ions near the cathode and the creation of a local charged zone termed the Chazalviel layer, is readily seen. Figure 2 shows details of the stationary state of the run in Fig. 1 and Fig. 3 shows the same as in Fig. 2 but for $\mathrm{Po}_A(\mathrm{Po}_C)=4.42\times10^{-4}$ (here $C_0=1\times10^{11}$ $1/\mathrm{cm}^3$). This produces a sharper curvature of the electrostatic potential and a narrow Chazalviel layer. Finally, Figs. 4(a), 4(b), and 4(c) show space-time contour plots for anion and cation concentrations and electrostatic potential, for the run in Fig. 1. This figure, as well as Fig. 1, illustrates the evolution of the solution towards its steady state; the building up of the Chazalviel layer constitutes a typical example of a singular perturbation problem. An imaginary cross section of Fig. 4(a) or 4(b) with a plane $(x=x_i,t)$ near the anodes, will show a higher than C_0 ion concentration front advancing with a velocity proportional to the square root of time.

The computations shown above are in accordance with analytical and numerical results presented in [15]. The difference here lies in the computational method used and in the absence of numerical oscillations (for the range of dimensionless numbers used here). This yields a robust numerical algorithm. The value of $\mathrm{Po}_A(\mathrm{Po}_C)$ used is far above the real one. For the real value, the Chazalviel layer is reduced to a step function in the electric potential which cannot be resolved with the grid used, and thus renders the algorithm ill conditioned (generation of numerical oscillations and instability). To partially overcome this problem we are currently developing an adaptive grid algorithm. In spite of its obvious limitations, the results of the 1D model shown above give a clear insight into the real problem of ECD.

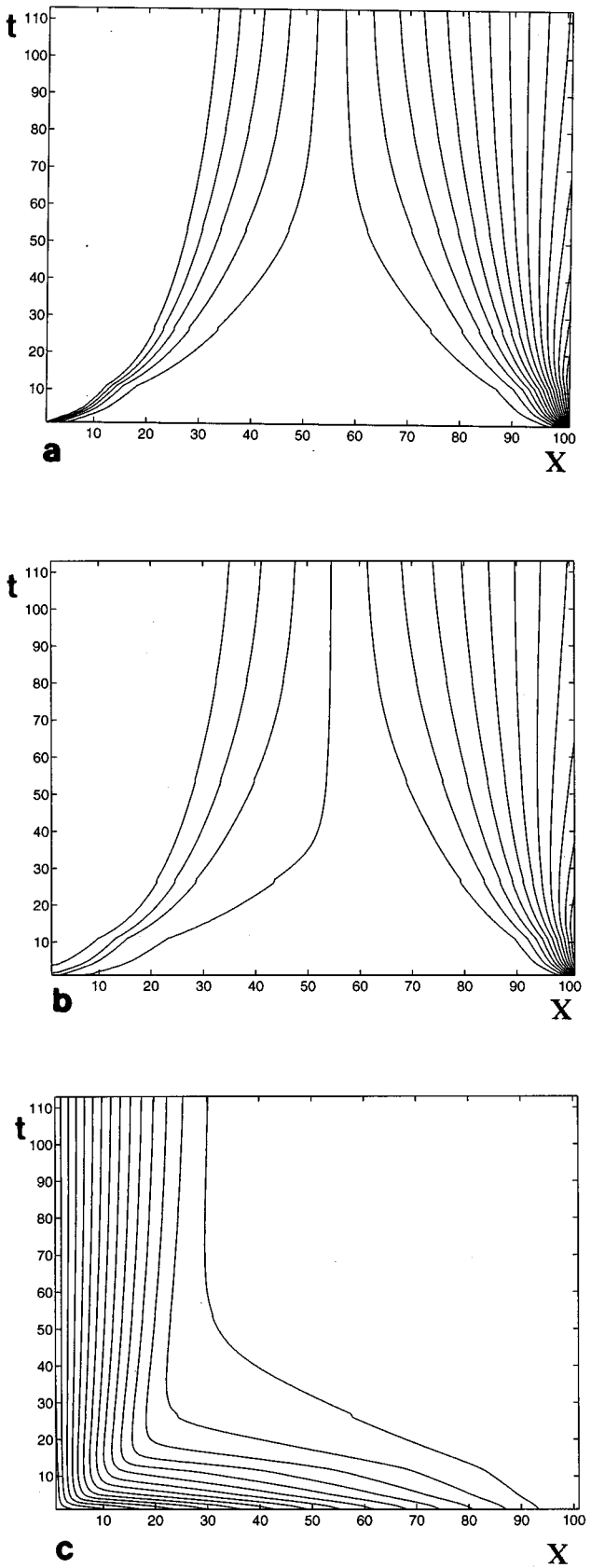

FIG. 4. Space-time contour plots for: (a) anion concentration, (b) cation concentration, and (c) electrostatic potential. The parameters are the same as in Fig. 1.

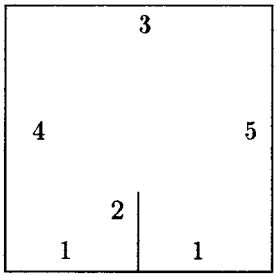

FIG. 5. Sketch of the computational domain.

V. A TWO-DIMENSIONAL APPROXIMATION WITH FIXED ELECTRODES

Studies of the ramified electrodeposit growth aim mainly to establish the relation between the driving nonlinear field and the morphology of the deposit. Here, to simulate this relation we use the experimental results presented in [20] and [22] as a guide. In a first step, as in [15], we assume a dense parallel morphology for the ramified electrodeposit and we study the distribution of concentrations, electrostatic potential, and fluid velocities. The deposit is replaced by a set of parallel spaced rectilinear filaments in the form of a comb and only one filament of the comb is analyzed by symmetry. The problem is described by system (11)–(15) in the 2D domain shown in Fig. 5.

Two different cases corresponding to two different scales will be considered.The first case corresponds to a simulation of the whole cell, the second one to a small region near the tip of the filament. For the first case the boundary conditions for (x,y) at sides 1 and 2 (corresponding to the cathode and the deposit) are

$$\phi(x,y) = -\frac{kT}{z_C e \phi_0} \ln[z_C C(x,y)], \tag{31}$$

$$\frac{\partial C}{\partial n}(x,y) = 0, \tag{32}$$

$$j_{An}(x,y) = -\frac{1}{\mathrm{Re}\, M_C} \frac{\partial A(x,y)}{\partial n} + \frac{1}{\mathrm{Re}\, \mathrm{Sc}_C} A(x,y) \frac{\partial \phi(x,y)}{\partial n} = 0, \tag{33}$$

where $j_{An}(x,y)$ is the anion flux and n is the normal to the boundary. For (x,y) on side 3 (corresponding to the anode), the boundary conditions are

$$\phi(x,y) = 1 - \frac{kT}{z_C e \phi_0} \ln[z_C C(x,y)], \tag{34}$$

$$C(x,y) = A(x,y) \tag{35}$$

$$j_{An}(x,y) = -\frac{1}{\mathrm{Re}\,M_C}\frac{\partial A(x,y)}{\partial n} + \frac{1}{\mathrm{Re}\,\mathrm{Sc}_C}A(x,y)\frac{\partial \phi(x,y)}{\partial n} = 0. \tag{36}$$

For (x,y) at sides 4 and 5 (corresponding to the lateral sides), the boundary conditions are

$$\frac{\partial C}{\partial n} = \frac{\partial A}{\partial n} = \frac{\partial \phi}{\partial n} = 0.$$

The boundary conditions for the stream function on every solid boundary are

$$\psi = \frac{\partial \psi}{\partial n} = 0.$$

For the second case, imagining now that Fig. 5 represents a small region near the tip of the filament, the boundary conditions for (x,y) on side 1 are

$$\frac{\partial C}{\partial n} = \frac{\partial A}{\partial n} = \frac{\partial \phi}{\partial n} = 0.$$

For (x,y) on side 3, the boundary conditions are

$$C = A = 1, \quad \frac{\partial \phi}{\partial n} = 0.$$

The remaining boundary conditions are the same as in the preceding case.

The computational model solves system (11)–(15), for each time step, in a fixed domain, in a lattice using finite differences and deterministic relaxation techniques in a similar way to the one described for the 1D approximation. Its solution is obtained via the system of difference equations

$$\mathbf{W}_k^{n+1} = \sum_j \mathbf{a}_j \mathbf{W}_j^n, \tag{37}$$

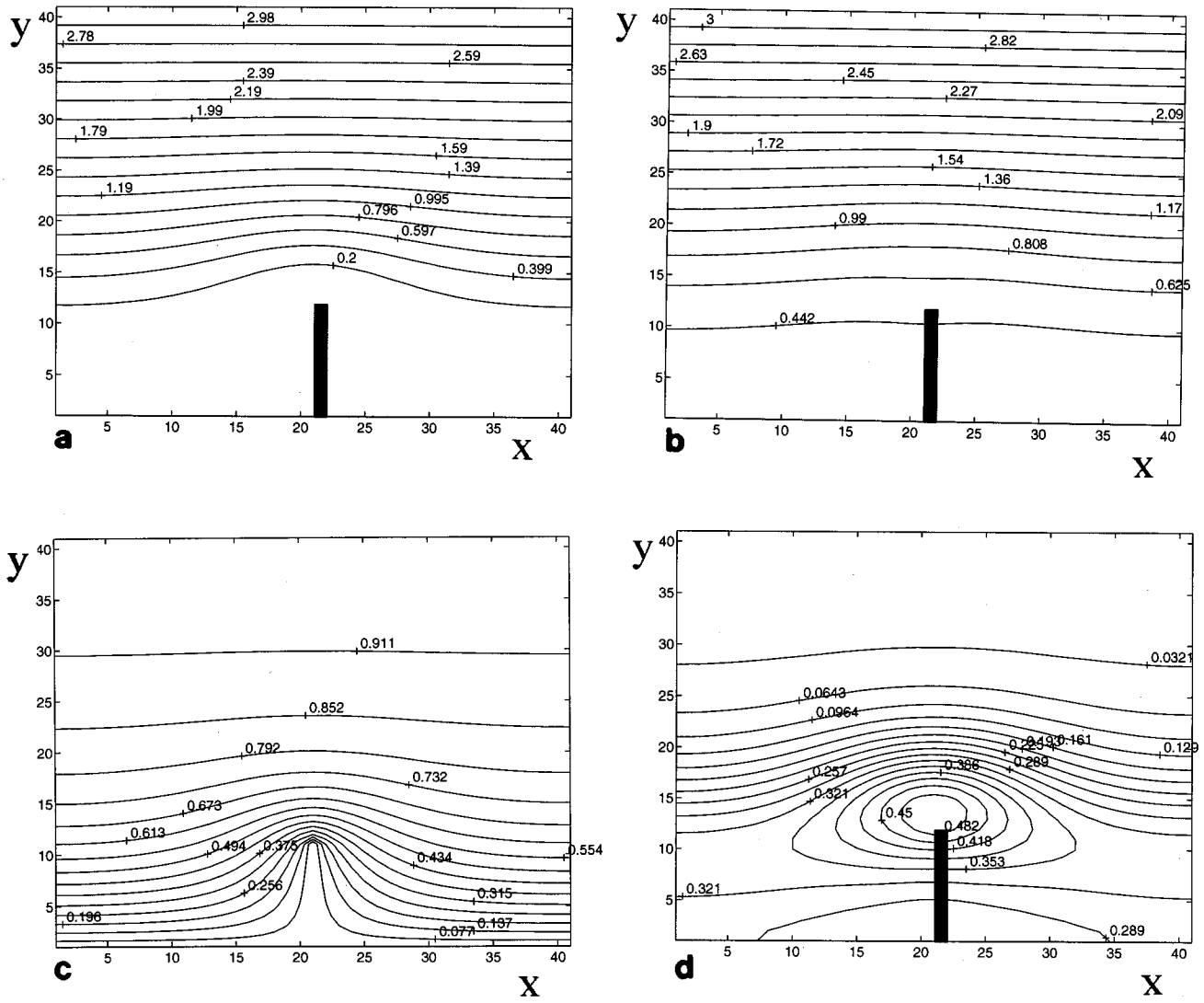

FIG. 6. Simulation of the whole cell without fluid flow and with one filament fixed at the cathode. Steady state contour lines for (a) anion concentration, (b) cation concentration, (c) electrostatic potential, and (d) forcing function f [$\mathrm{Sc}_C(\mathrm{Sc}_A) = 10^2$, $M_A = 12.06$, $M_C = 18.62$, and $\mathrm{Po}_A(\mathrm{Po}_C) = 4.43 \times 10^{-2}$].

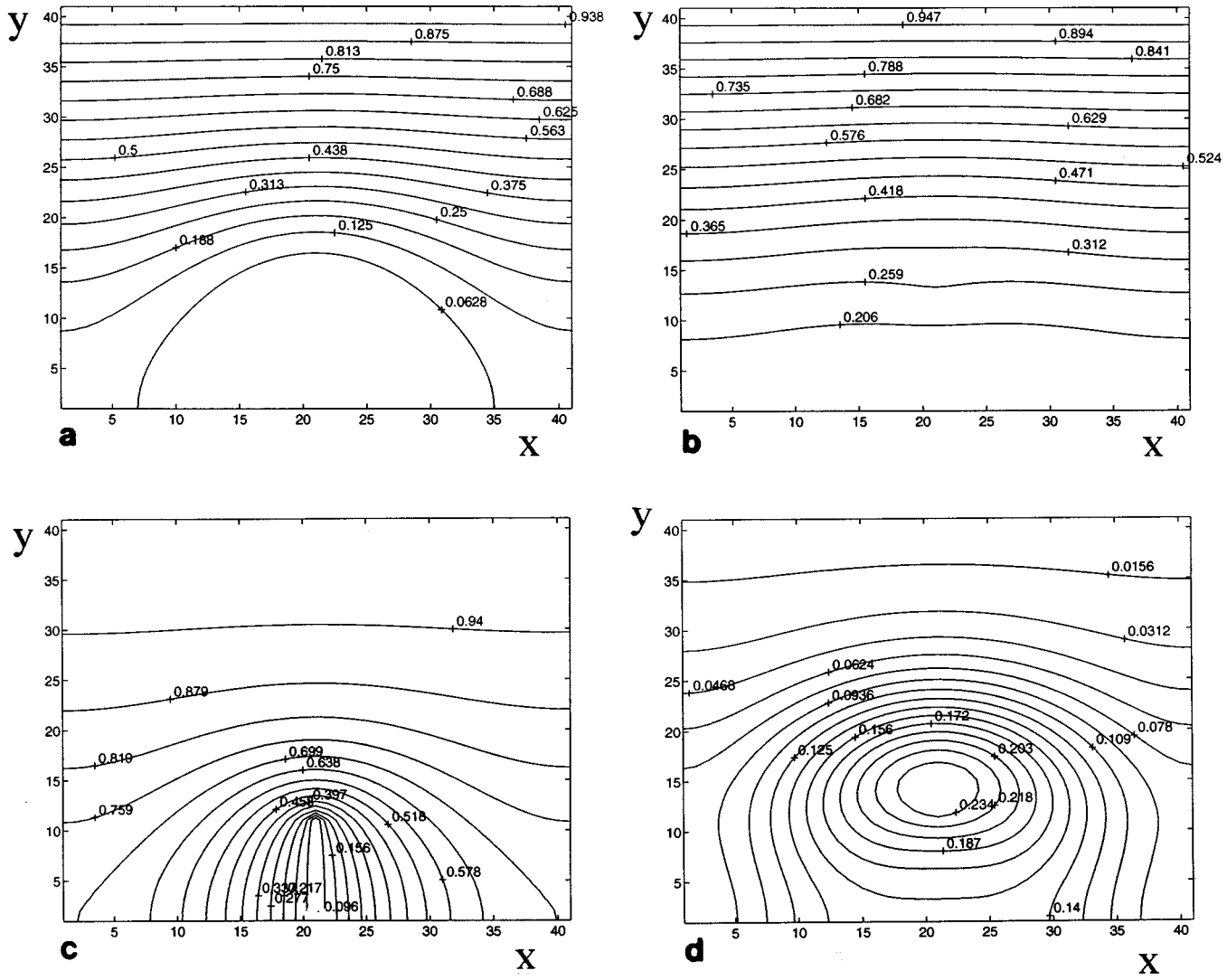

FIG. 7. Simulation of a small region near the tip of a fixed filament without fluid flow. Steady state contour lines for (a) anion concentration, (b) cation concentration, (c) electrostatic potential, and (d) forcing function f [$\mathrm{Sc}_C(\mathrm{Sc}_A)=10^2$, $M_A=12.06$, $M_C=18.62$, and $\mathrm{Po}_A(\mathrm{Po}_C)=4.43\times10^{-2}$].

where j represents the nearest-neighbor site of the site k, the summation ranges over all nearest-neighbor sites, $\mathbf{W}_k$ is a vector valued function, whose components are the concentrations C and A, the electrostatic potential ϕ, the vorticity function ω and the stream function ψ, and $\mathbf{a}_j$ is a diagonal matrix whose elements contain the nonlinear coefficients of the discretized equations.

A simulation of the whole cell without fluid flow and with one fixed filament representing a grown deposit on the cathode is shown next. We use a grid of 40×40 cells, and the following dimensionless numbers: $\mathrm{Sc}_C(\mathrm{Sc}_A)=10^2$, $M_A=12.06$, $M_C=18.62$, and $\mathrm{Po}_A(\mathrm{Po}_C)=4.43\times10^{-2}$. Figures 6(a), 6(b), 6(c), and 6(d) show steady state contour lines for anion and cation concentrations, electrostatic potential and forcing function f. The forcing function f possesses an almost compact support, i.e., an approximately bounded domain of (x,y) in which its value is not negligible; this domain is near the tip of the filament, as predicted by theory and demonstrated by experiments. Note that the contour lines are symmetric with respect to the computational filament, that in the figure was superimposed slightly off center.

The simulation of a small region near the tip of a fixed filament without fluid flow is presented next. Figures 7(a), 7(b), 7(c), and 7(d) show steady state contour lines for anion and cation concentrations, electrostatic potential and forcing function f. Comparing these results with those of Fig. 6 we see that the former corresponds to a small window near the tip of the deposit in Fig. 6. This is obtained by changing the boundary conditions as described earlier.

We turn now to the simulation of a small region near the tip of a fixed filament with fluid flow.The dimensionless numbers are $\mathrm{Re}=10$, $\mathrm{Sc}_C(\mathrm{Sc}_A)=10^2$, $M_A=12.06$, $M_C=18.62$, $\mathrm{Po}_A(\mathrm{Po}_C)=4.43\times10^{-2}$, $\mathrm{Fr}_C(\mathrm{Fr}_A)=6.25$. Figures 8(a), 8(b), 8(c), 8(d), and 8(e) show steady state contour lines for anion and cation concentrations, forcing function f, electrostatic potential and stream function. The presence of the fluid is manifested by the appearance of a pair of contrarotative vortices in Fig. 8(e). A comparison of Fig. 8 with Fig. 7 shows that the influence of the fluid over the system is very weak, due to the high value of the Fr number used. To see a larger influence we show next similar results but for a small Fr number; this implies the use of a lighter

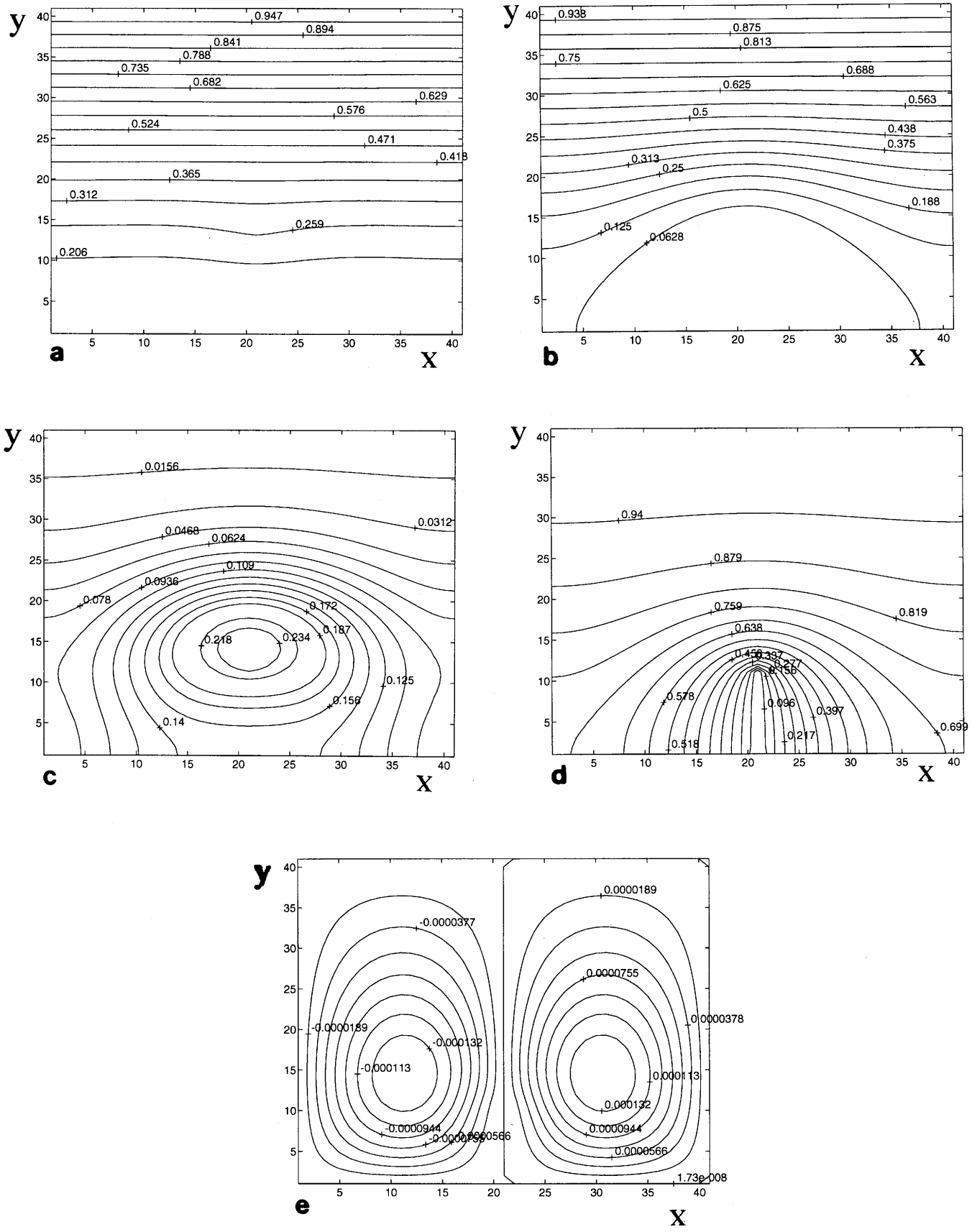

FIG. 8. Simulation of a small region near the tip of a fixed filament with fluid flow. Steady state contour lines for (a) anion concentration, (b) cation concentration, (c) forcing function, (d) electrostatic potential, and (e) stream function. Re=10, $\mathrm{Sc}_C(\mathrm{Sc}_A)=10^2$, $M_A=12.06$, $M_C=18.62$, $\mathrm{Po}_A(\mathrm{Po}_C)=4.43\times10^{-2}$, $\mathrm{Fr}_C(\mathrm{Fr}_A)=6.25$.

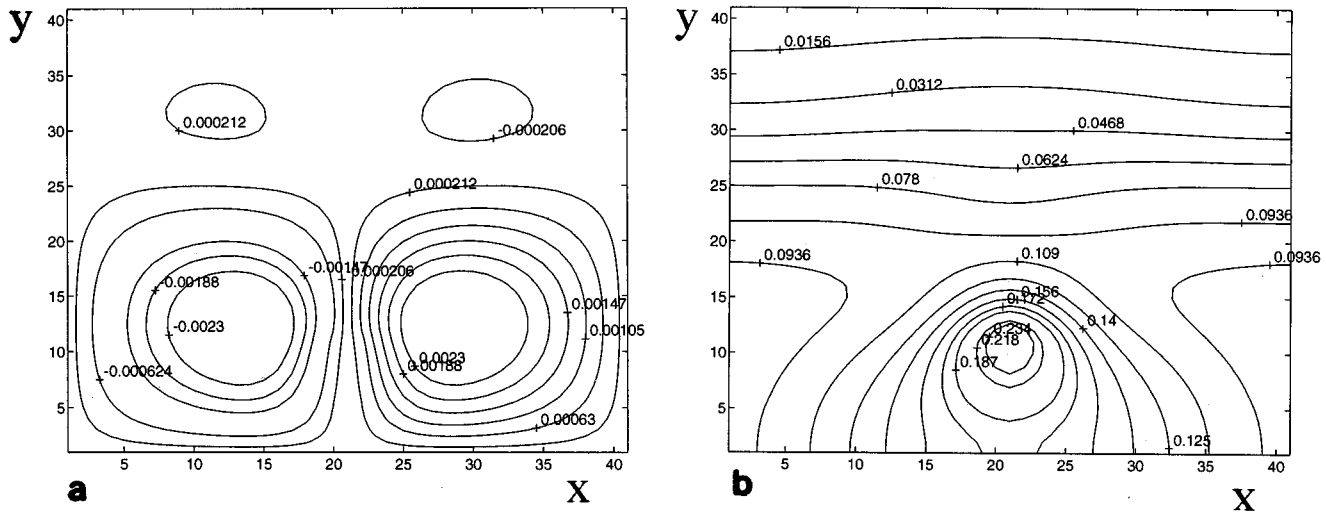

FIG. 9. Simulation of a small region near the tip of a fixed filament with fluid flow. Steady state contour lines for (a) stream function and (b) forcing function (same parameters as Fig. 8 but with Fr=0.05).

and less viscous fluid. Figures 9(a) and 9(b) show contours of stream function and forcing function for Fr=0.05. A comparison between Fig. 9(a) and Fig. 8(e) reveals that a decrease in the Fr number produces higher vorticity, stream function gradients and thus velocities. A similar comparison between forcing functions shows that a decrease in the Fr number increases the gradient of the forcing function (reduces the support of the forcing function). Thus higher gradients of the forcing functions or higher velocities narrow the Chazalviel layer.

The main result here is that the local space charge produces a pair of contrarotative vortices near the tip of the deposit. The right vortex is counter clockwise and positive by convention. The local space charge has an almost compact support, that is, a small region near the tip where the difference between cations and anions is not negligible. Therefore, the vortex extension and amplitude are modulated by that difference and by the Fr number, respectively, assuming a constant Re number. Clearly, the presence of electroconvection decreases the size of the Chazalviel layer, and thus of the compact support of the space charge.

VI. A TWO-DIMENSIONAL GROWTH MODEL APPROXIMATION

The final step (for the present work) towards a more realistic description of ECD with dense-branched morphology is the inclusion of the growth mechanism that yields ramified deposits. Fluid motion in a typical ECD experiment arises primarily from electric fields combined with buoyancy effects. During the first stages of the process the initial instability yielding ramified deposits could be triggered at random locations by the perturbation of the Coulomb forces due to gravity currents. To mimic this process (in the absence of buoyancy effects) the following growth model approximation is proposed. The instability is triggered at random locations near the cathode or the deposit. That is, the interface of the deposit moves at random with a stochastic rule. This rule is an extension of a DBM scheme introduced in [8] and consists in moving the interface at random proportionately to the flux of cations. The flux of cations at the interface is obtained through the solution of the ECD system (11)–(15) in the initial domain indicated in Fig. 5, with initial and boundary conditions similar to those of the preceding section. Clearly, our main assumption is that the flux of cations entering the deposit governs the aggregation process.

The computational model assumes an initial configuration and solves system (11)–(15), for each time step, in a fixed domain, in a lattice using finite differences and deterministic relaxation techniques in a similar way to the one described for the 2D approximation. The resulting solution $\mathbf{W}_k^{n+1}$ is then used to modify the domain (advance the interface) with a DBM scheme [8]. This consists in moving the interface at random proportionately to the flux of cations, i.e.,

$$p_k=\frac{|\mathbf{j}_{ck}|}{\sum_i |\mathbf{j}_{ci}|}, \tag{38}$$

where k is a nearest-neighbor site to the interface, p_k is the probability of selecting the nearest neighbor site k to advance the interface, and the summation is over all nearest-neighbor sites i to the interface, $\mathbf{j}_{ck}$ is the flux of cations flowing from the neighbor site k into the aggregation.

In this process each new advancement of the interface changes locally the boundary and hence the solution of system (11)–(15), that must be recalculated, in principle, at every time step. In this way the aggregation process, the ionic species, the electric field and the hydrodynamics are coupled. In summary, the computational interface growth or aggregation process consists in adding a new cell at random according to the stochastic rule given in the preceding equation.

The results that follow aim to describe qualitatively the evolution of the interface as an interplay of the main transport mechanisms near the tips of the aggregation: fluid dif-

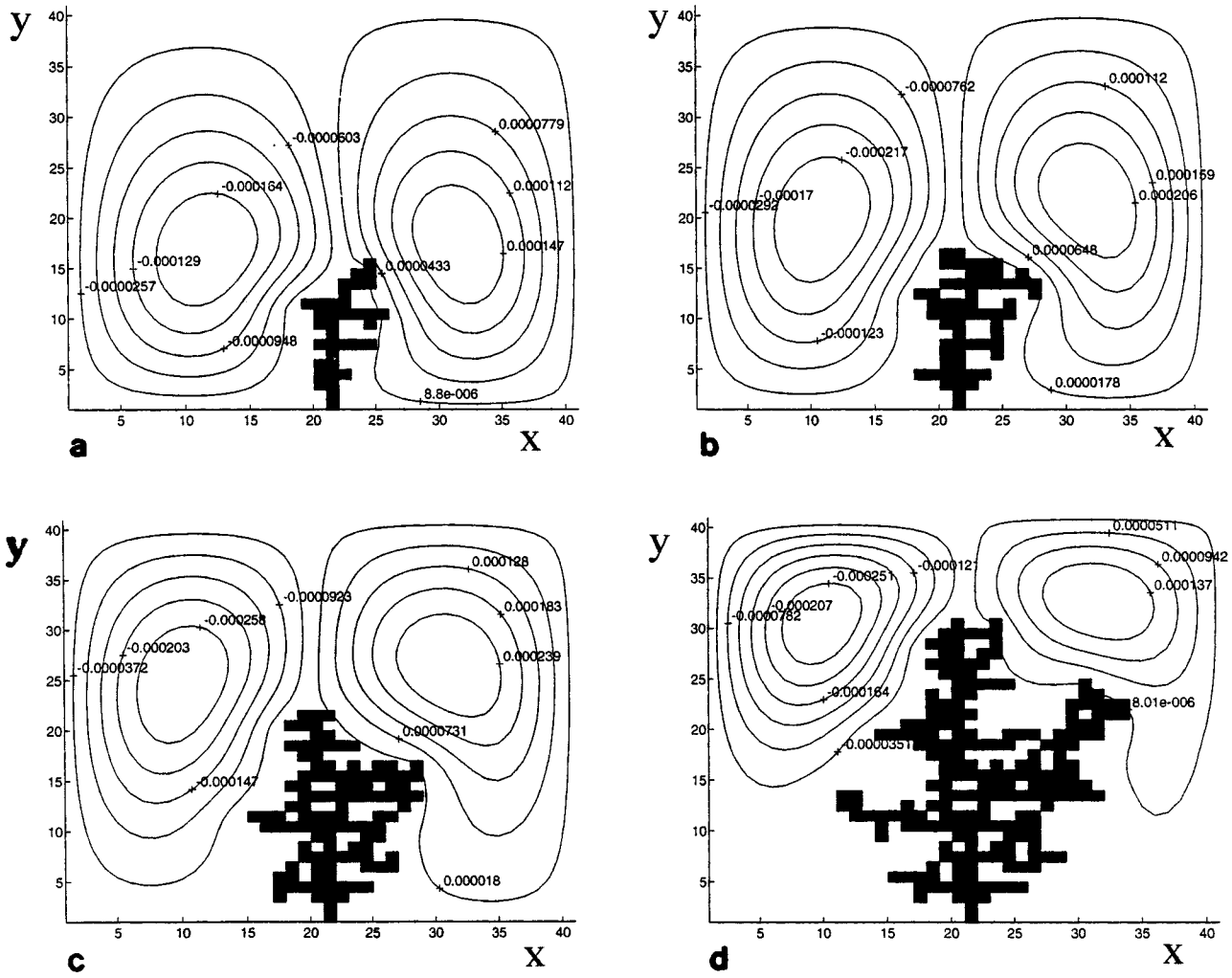

FIG. 10. Simulation of the growth in a small region near the tip of one filament. Snapshots of aggregation superimposed to stream function for (a) 250 sec, (b) 500 sec, (c) 1000 sec, and (d) 2000 sec [Re=10, $\mathrm{Sc}_C(\mathrm{Sc}_A)=100$, $M_A=12.06$, $M_C=18.62$, $\mathrm{Po}_A(\mathrm{Po}_C)=0.0443$, $\mathrm{Fr}_C(\mathrm{Fr}_A)=6.25$].

fusion and convection, ion migration, diffusion and convection, following as close as possible the experimental conditions presented in [20,22]. Initially, the fluid is at rest, there is no aggregation except at the bottom layer, where the initial instability is mimicked with a deposit of 11 occupied cells; the voltage varies linearly from 1 at the top (anode) to 0 at the bottom and the deposit.

A simulation of growth in a small region near the tip of one filament is shown next. The region is represented by a grid of 41×41 cells. The dimensionless numbers used are Re=10, $\mathrm{Sc}_C(\mathrm{Sc}_A)=100$, $M_A=12.06$, $M_C=18.62$, $\mathrm{Po}_A(\mathrm{Po}_C)=0.0443$ (for numerical stability we have chosen $C_0=1\times10^9$ 1/cm^3, $D_A(D_C)=1\times10^{-4}$ cm^2/sec) and $\mathrm{Fr}_C(\mathrm{Fr}_A)=6.25$. Figure 10 shows a sequence of vortex-tip interactions for different times: (a) 250 sec, (b) 500 sec, (c) 1000 sec, and (d) 2000 sec; the time step is 10 sec and the aggregation speed is $m=1$ cell-time step. Here, by aggregation speed m we mean the number of cells aggregated per unit of time. In Fig. 10(a) the tip of the deposit stochastically bends to its right, pinching the adjacent vortex [Fig. 10(b)] more pronouncedly. Fanning [30] is a mechanism by which the action of the convective flow deforms the tip of the branch in such a way that tip splitting can take place. In our growth model fanning is mimicked with a stochastic process. Figure 10(c) depicts the deformation of the tip due to the action of the right vortex that yields tip splitting and the birth of two new branches in Fig. 10(d). In this last frame one of the child branches pinches the right vortex that will split (die) in a later time, giving birth to two baby vortices (not shown here). Trees bend because of the vortex influence producing a screening effect in the neighborhood (lower branches stop growing, i.e., they die).

Figures 11(a), 11(b), 11(c), and 11(d) show a snapshot at 2000 sec of the contour lines and aggregation for cation and anion concentrations, electrostatic potential and forcing function f. Consider for one moment Fig. 10(c) and Fig. 10(d) as a simultaneous growth of two adjacent trees and let us imaginarily join these two neighboring filaments with an arch containing the positive vortex of the left tip and the negative vortex of the right tip. The inner zone of this arch is depleted of ions while the outer zone rapidly reaches the bulk concentration value [as shown in Figs. 11(a) and 11(b)].

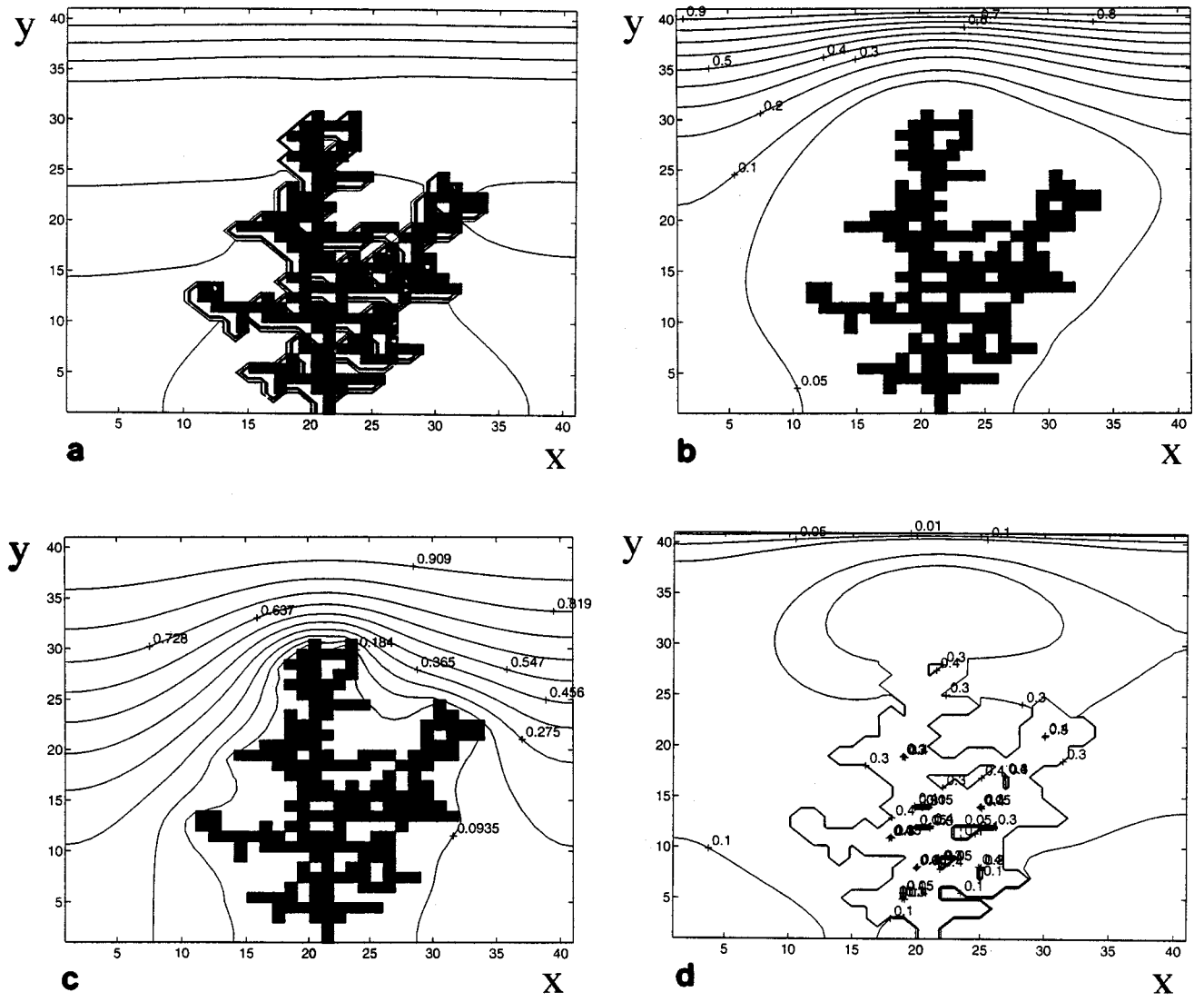

FIG. 11. Simulation of the growth in a small region near the tip of one filament. Snapshots at 2000 sec of aggregation superimposed to (a) cation concentration, (b) anion concentration, (c) electrostatic potential, and (d) forcing function f (same parameters as in Fig. 10).

We consider now the influence on the growth model of a variation in the Fr number and in the aggregation speed m. The DBM scheme advances the interface at random proportionately to the flux of cations. When Coulomb forces and electroconvection increase, the flux distribution at the tip of the filament increases too. By construction, the probability of moving the interface and the aggregation process increase at the tip. Therefore, in theory and for many time steps and very fine grids, aggregation is enhanced at the tip. In practice, however, the coarse grid used in space and time introduces fluctuations which yield results departing from theory. To smooth these fluctuations we sample m times with the same flux distribution, that is, we advance m positions per time step. Figure 12 shows snapshots of the deposit with 1000 particles, for Fr$=6.25$ and (a) $m=10$, (b) $m=50$, (c) $m=100$, and (d) $m=200$; Fig. 13 shows the same but for Fr$=0.01$. Comparing in Figs. 12 and 13 deposits for equal m we see that the influence of the Fr number is weak but increases with m. For instance, the comparison of Fig. 12(d) and Fig. 13(d), shows in the latter a tendency to grow upwards and be more slender for reasons discussed earlier. Higher m reduces the stochasticity of the system (a deeper analysis of the influence of the parameter m in the morphology of the deposit is deemed relevant and it is being pursued elsewhere). This result is in accordance with the experiments presented in [30] showing that at higher growth speeds, i.e., larger Coulomb forces, the filament growth is thinner and straighter due to vortex action.

The results of Fig. 12 and 13 show subtle changes in the structure of the deposit as a function of Coulomb forces (the Fr number). This is because the variation of the flux at the interface with Coulomb forces is very small for the range of parameters used here. In addition, there is an artificial viscosity (due to the coarseness of the grid used) that yields velocities at the interface smaller than those corresponding to the Re number used. The use of denser grids diminishes this effect but is excluded due to computer limitations. To circumvent this problem we propose the following mechanism. We consider m as a function of Coulomb forces. For instance, $m=\alpha/\mathrm{Fr}$, where $1<\alpha<100$ is an adjustment param-

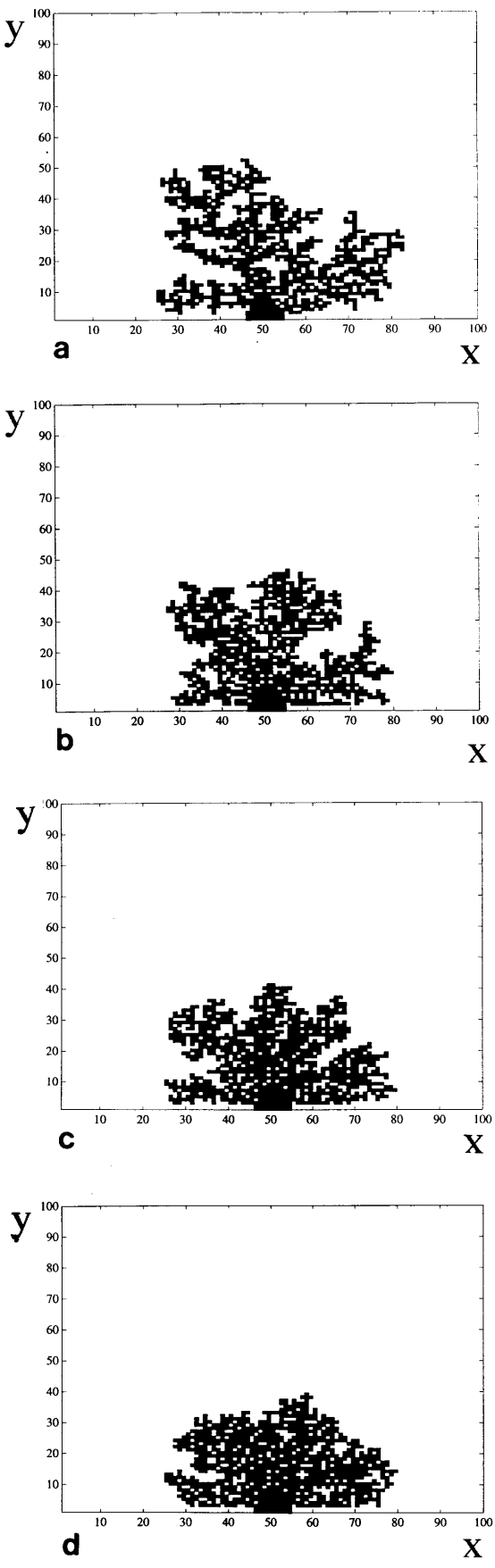

FIG. 12. Snapshots of the deposit with 1000 particles, for Fr $=6.25$ and (a) $m=10$, (b) $m=50$, (c) $m=100$, and (d) $m=200$.

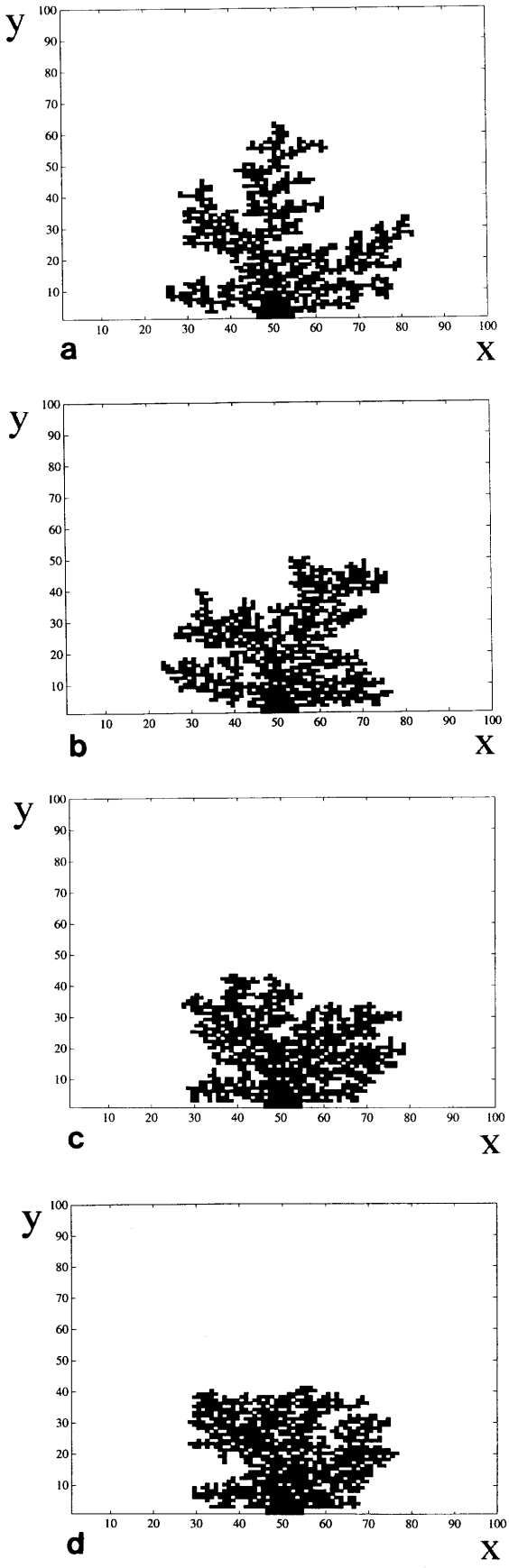

FIG. 13. Snapshots of the deposit with 1000 particles, for Fr $=0.01$ and (a) $m=10$, (b) $m=50$, (c) $m=100$, and (d) $m=200$.

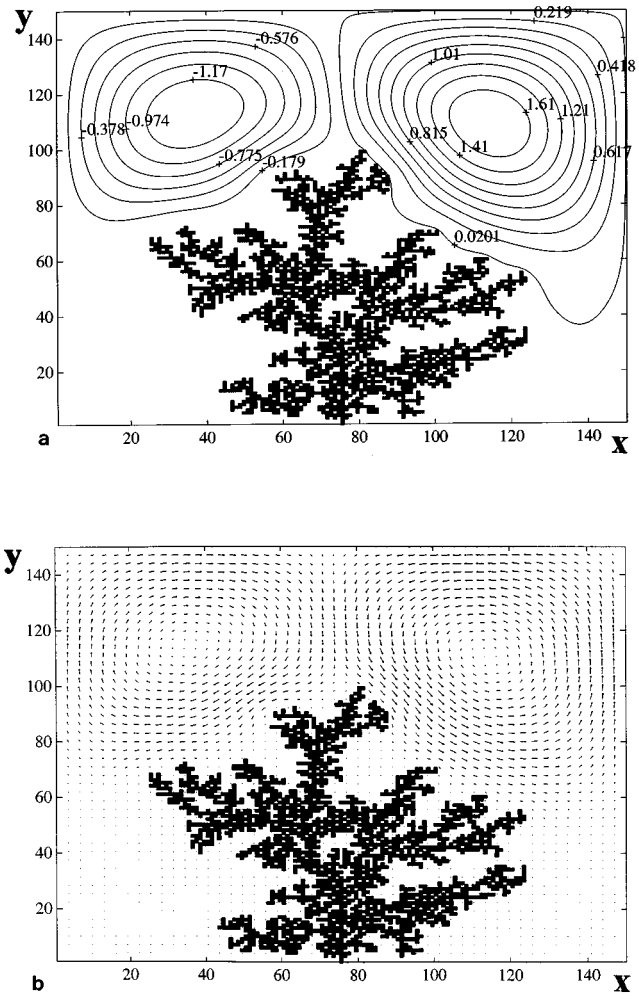

FIG. 14. Simulation of the growth in a small region near the tip of one filament. Snapshots at $t=20\,000$ sec of (a) deposit and stream function contours (multiplied by 10^4) and (b) deposit and velocity map (same parameters as in Fig. 10 but for a grid of 150 $\times$150 cells).

eter. So for $\alpha=2$ and Fr=0.01, $m=200$ and for $\alpha=62.5$, Fr=6.25, $m=10$. In this context, comparing the growth of Fig. 12(a) with that of Fig. 13(d) for Fr=0.01, we see that the influence of this number is much sharper, that is, larger Coulomb forces (lower Fr numbers) yield taller and more slender aggregates. These results suggest that an increase in the Fr number produces deposits with more side branching.

Finally, the simulation of growth in a small region near the tip of one filament in a grid of 150$\times$150 cells is shown. The parameters are the same as in previous runs, but for Fr=6.25 and $m=1$. Figure 14 depicts snapshots at $t=20\,000$ sec for (a) deposit and stream function contours and (b) deposit and velocity map. These results reveal a streamline pattern with a pair of contrarotative vortices and a funnellike shape through which the copper ions are sucked into the tip. Behind the vortices the fluid is at rest.

VII. CONCLUSIONS

We presented theoretical and numerical results of a macroscopic model for the study of ECD in a 2D linear cell with a constant potential between electrodes. Our aim was to approximately describe dense-branched morphology experiments presented in the literature, whose growth is governed by the coupled effects of diffusion, migration, and electroconvection. With a proper variation of the set of dimensionless numbers introduced it is possible to obtain a streamline pattern showing the existence of local charges near the tips of the filaments, the associated pair of contrarotating vortices and a funnellike shape through which the cations are sucked into the tip. The genesis of the ramified deposit is elucidated through the analysis of the evolution of the vortex-tip interaction. This evolution shows the stretching and division of vortices and the concomitant birth, splitting, fanning, and death of tip filaments. There is a reasonably qualitative agreement between the streamline, ion concentrations, and electrostatic potential computational results and the experimental results presented in the literature.

ACKNOWLEDGMENTS

We are indebted to J. de Bruyn, J. N. Chazalviel, V. Fleury, S. Morris, M. Olivella, and B. Sapoval for enlightening discussions. This work was partially supported by CONICET Project PIA-369/92 and UBA Project EX233/95. G.M. gratefully acknowledges the financial support of the Thalmann Foundation. P.M. acknowledges the financial support of the UBA.

[1] B. B. Mandelbrot, *The Fractal Geometry of Nature* (Freeman, San Francisco, 1982).
[2] T. Vicsek, *Fractal Growth Phenomena* 2nd ed. (World Scientific, Singapore, 1992).
[3] *On Growth and Form,* Vol. 100 of NATO *Advanced Study Institute, Ser. B: Physics*, edited by G. Stanley and N. Ostrowsky (Kluwer, Boston, 1986).
[4] L. Kadanoff, J. Stat. Phys. **39**, 267 (1985).
[5] F. Argoul, J. Huth, P. Merzeau, A. Arneodo, and H. L. Swinney, Physica D **62**, 170 (1993).
[6] J. S. Newman, *Electrochemical Systems* (Prentice Hall, New Jersey, 1973).
[7] T. A. Witten and L. M. Sander, Phys. Rev. B **27**, 5686 (1983).
[8] L. Pietronero and H. J. Weismann, J. Stat. Phys. **36**, 909 (1984).
[9] P. Meakin, Phys. Rev. B. **28**, 5221 (1983).
[10] G. Marshall, Comput. Phys. Commun. **56**, 51 (1989).
[11] G. Marshall (unpublished).
[12] L. Lam, R. D. Pochy, and V. M. Castillo, in *Nonlinear Structures in Physical Systems*, edited by L. Lam and H. C. Morris (Springer, New York, 1990).
[13] G. Marshall and E. Arguijo, Chaos, Solitons Fractals **5**, 531 (1992).
[14] G. Marshall, S. Tagtachian, and L. Lam, Chaos, Solitons Fractals **6**, 325 (1995).
[15] J. N. Chazalviel, Phys. Rev. E **42**, 7355 (1990).

[16] J. R. Melrose, D. B. Hibbert, and R. C. Ball, Phys. Rev. Lett. **65**, 3009 (1990).
[17] V. Fleury, J. N. Chazalviel, M. Rosso, and B. Sapoval, Phys. Rev. A **44**, 6693 (1991).
[18] V. Fleury, M. Rosso, and J. N. Chazalviel, Phys. Rev. A **43**, 6908 (1991).
[19] V. Fleury, J. N. Chazalviel, and M. Rosso, Phys. Rev. Lett. **68**, 2492 (1992).
[20] V. Fleury, J. N. Chazalviel, and M. Rosso, Phys. Rev. E **48**, 1279 (1993).
[21] P. P. Trigueros, F. Mas, J. Claret, and F. Sagues, J. Electroanal. **348**, 221 (1993).
[22] V. Fleury, J. Kaufman, and B. Hibbert, Nature **367**, 435 (1994).
[23] D. Barkey, J. Electrochem. Soc. **138**, 2912 (1991).
[24] R. H. Kork, D. C. Pritchard, and W. Y. Tam, Phys. Rev. A **44**, 6940 (1991).
[25] M. Wang and N. Ming, Phys. Rev. A **45**, 2493 (1992).
[26] A. Kuhn and F. Argoul, Fractals **3**, 451 (1993).
[27] C. Livermore and Po-zen Wong, Phys. Rev. Lett. **72**, 3847 (1994).
[28] K. A. Linehan and J. R. de Bruyn, Can. J. Phys. **73**, 177 (1995).
[29] D. Otero, G. Marshall, and S. Tagtachian, Fractals **4**, 7 (1996).
[30] V. Fleury, J. Kaufman, and B. Hibbert, Phys. Rev. E **48**, 3831 (1993).
[31] J. Huth, H. L. Swinney, W. D. McCormick, A. Kuhn, and F. Argoul, Phys. Rev. E **51**, 3444 (1995).
[32] G. Marshall, E. Perone, P. Tarela, and P. Mocskos, Chaos, Solitons Fractals **6**, 315 (1995).
[33] R. Bruinsma and S. Alexander, J. Chem. Phys. **92**, 3075 (1990).
[34] I. Rubinstein, *Electro-Diffusion of Ions* (SIAM Studies in Appl. Math., Philadelphia, 1990).
[35] Suzuki and Sawada, Phys. Rev. A **27**, 478 (1983).